Supplemental material

Bozzi et al., **https://doi.org/10.1085/jgp.201912428**

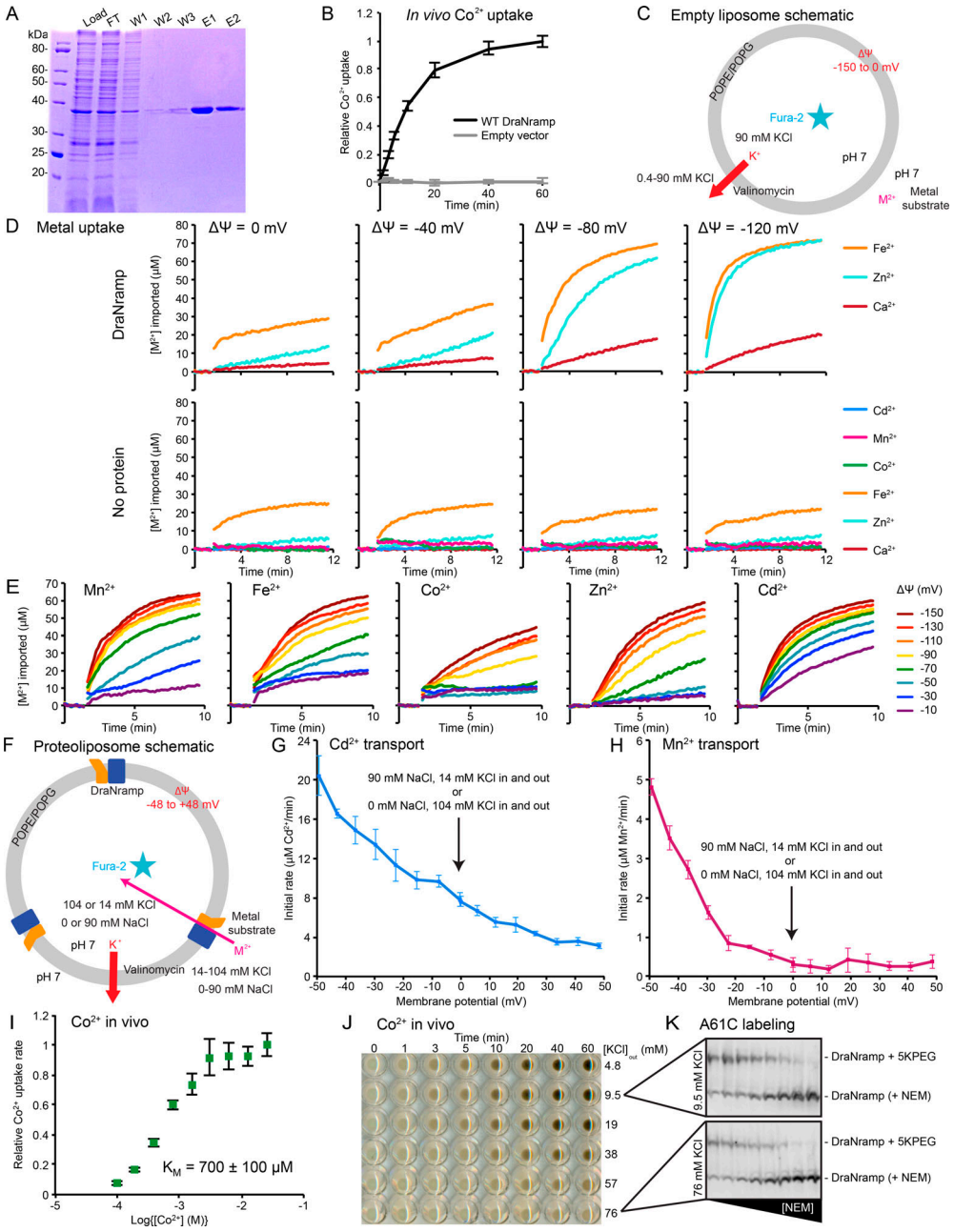

Figure S1. **DraNramp is a voltage-dependent transition metal transporter. (A)** Coomassie-stained SDS gel of His-tagged DraNramp purification via Ni^{2+}-affinity showing load, flow-through (FT), washes (W1, W2, W3), and elutions (E1, E2). **(B)** Colorimetric detection of Co^{2+} taken up by cells over time at pH 7.0 and 10 mM KCl shows that DraNramp transports Co^{2+} when expressed in *E. coli*. Data are averages ± SEM (n = 4). **(C)** Control liposomes lacking DraNramp are used to determine protein-dependent transport activity. **(D)** Representative time traces ($n \geq 4$) of metal uptake by DraNramp-containing liposomes (top) show that Fe^{2+} and Zn^{2+} also exhibit strong voltage dependence, while Ca^{2+} remains a poor substrate across all voltages. Control liposomes (bottom) have slow, but nonnegligible, voltage-independent Fe^{2+} and Zn^{2+} leak. **(E)** Representative time traces (n = 4) of metal uptake by DraNramp-containing liposomes at different membrane voltages. Transport of all five tested substrates is accelerated at high-magnitude negative membrane potentials, as also shown in Fig. 2 C. **(F)** Schematic for proteoliposome assays with moderate negative and positive ΔΨ values. Liposomes for $\Delta\Psi \leq 0$ contained only KCl inside and were diluted to a lower external $[K^+]$, with increased Na^+ used to balance osmolarity, before adding valinomycin to establish the membrane potential. Liposomes for $\Delta\Psi \geq 0$ contained mainly NaCl inside and were diluted into higher outside $[K^+]$. The pH was 7 on both sides of the membrane. **(G and H)** Average initial transport rate ± SEM (n = 4) versus membrane potential. Cd^{2+} transport (G) driven by a $[Cd^{2+}]$ gradient occurs even at $\Delta\Psi \geq 0$, although the rate decreases at more positive ΔΨ. In contrast, Mn^{2+} transport (H) does not occur unless $\Delta\Psi < 0$. Importantly, for both Cd^{2+} and Mn^{2+} at 0 mV, the observed transport behavior is the same regardless of whether the dominant cation species on both sides of the membrane is K^+ or Na^+. Thus, these ions on their own do not enable or inhibit transport, but rather the membrane potential causes the observed variations in transport rates. **(I)** Dose–response curve shows that Co^{2+} transport in *E. coli* has K_m = 700 ± 100 μM, similar to that obtained at ΔΨ = −150 mV in proteoliposomes, confirming that DraNramp behavior in vitro is physiologically relevant. Data are averages ± SEM (n = 4). Error in K_m is the uncertainty of fit to data. **(J)** Representative image of Co^{2+} uptake assay results showing that increased extracellular $[K^+]$ inhibits DraNramp-dependent Co^{2+} uptake in *E. coli*, as detected by precipitating transported Co^{2+} as the dark solid CoS. **(K)** Representative Western blots showing that A61C is labeled by NEM similarly in high or low external $[K^+]$.

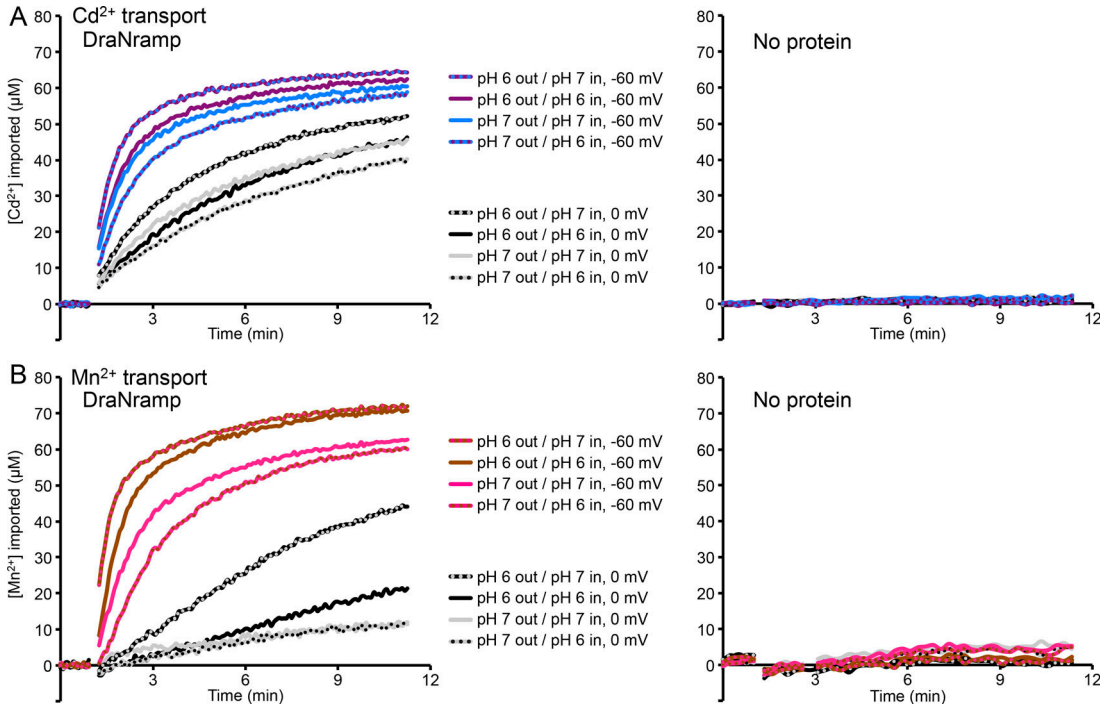

Figure S2. **pH gradients accelerate Cd^{2+} and Mn^{2+} transport. (A and B)** Representative time traces of 750 µM Cd^{2+} (A) or Mn^{2+} (B) uptake into proteoliposomes or empty liposomes ($n \geq 3$) at $\Delta\Psi = 0$ or −60 mV. A favorable ΔpH (6 outside/7 inside) accelerated metal uptake compared with no ΔpH (6 outside/6 inside or 7 outside/7 inside), while an unfavorable ΔpH (7 outside/6 inside) slowed metal uptake. Acidic pH without a pH gradient (6 outside/6 inside) also accelerated Mn^{2+} transport compared with external pH (7 outside/7 inside). This latter effect is not observed for Cd^{2+} transport. The righthand panels show that the various pH gradients did not enable metal uptake into empty liposomes.

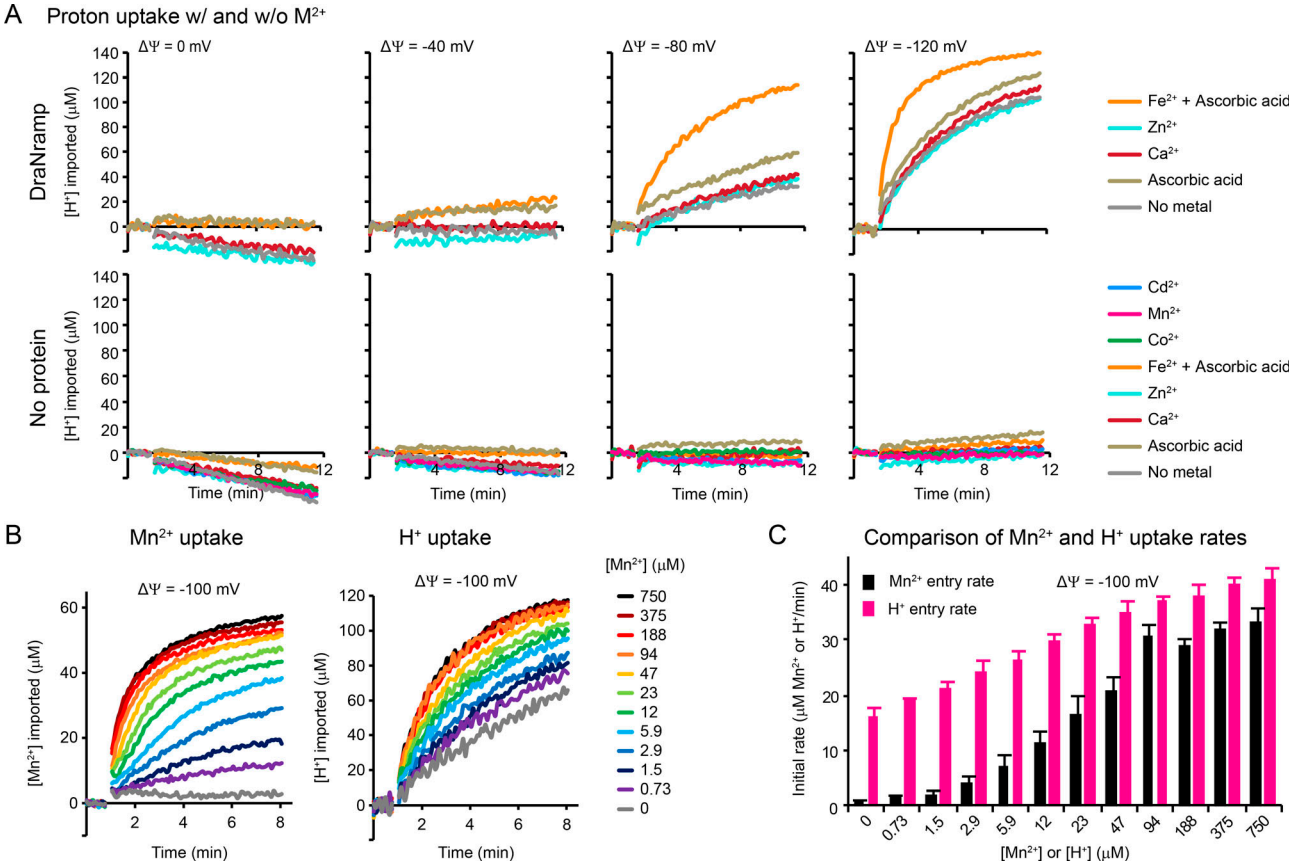

Figure S3. **Proton transport rates are metal specific. (A)** Representative time traces ($n \geq 4$) of H^+ uptake. Fe^{2+} stimulated H^+ entry into proteoliposomes (top), while Zn^{2+} (substrate) and Ca^{2+} (nonsubstrate) did not. ΔΨ-driven H^+ import was DraNramp dependent, as there was no significant H^+ leak or metal-stimulated H^+ entry into control liposomes (bottom). Ascorbic acid used to prevent Fe^{2+} oxidation slightly lowered the external pH, which led to slight proteoliposome acidification. Except for the reporter dye, conditions were identical to those for the metal transport in Fig. S1 D. **(B)** Representative time traces ($n = 3$) of Mn^{2+} and H^+ entry into proteoliposomes at ΔΨ = −100 mV with various $[Mn^{2+}]$ values. **(C)** Initial Mn^{2+} (black) and H^+ (magenta) uptake rates show that increasing $[Mn^{2+}]$ stimulated greater H^+ influx above its basal no-metal rate. Below a saturating Mn^{2+} concentration, the ratio of proton-to-metal transport deviated from 1:1, likely reflecting that some transporters underwent H^+ uniport while others performed Mn^{2+}:H^+ cotransport. Data are averages ± SEM ($n = 3$).

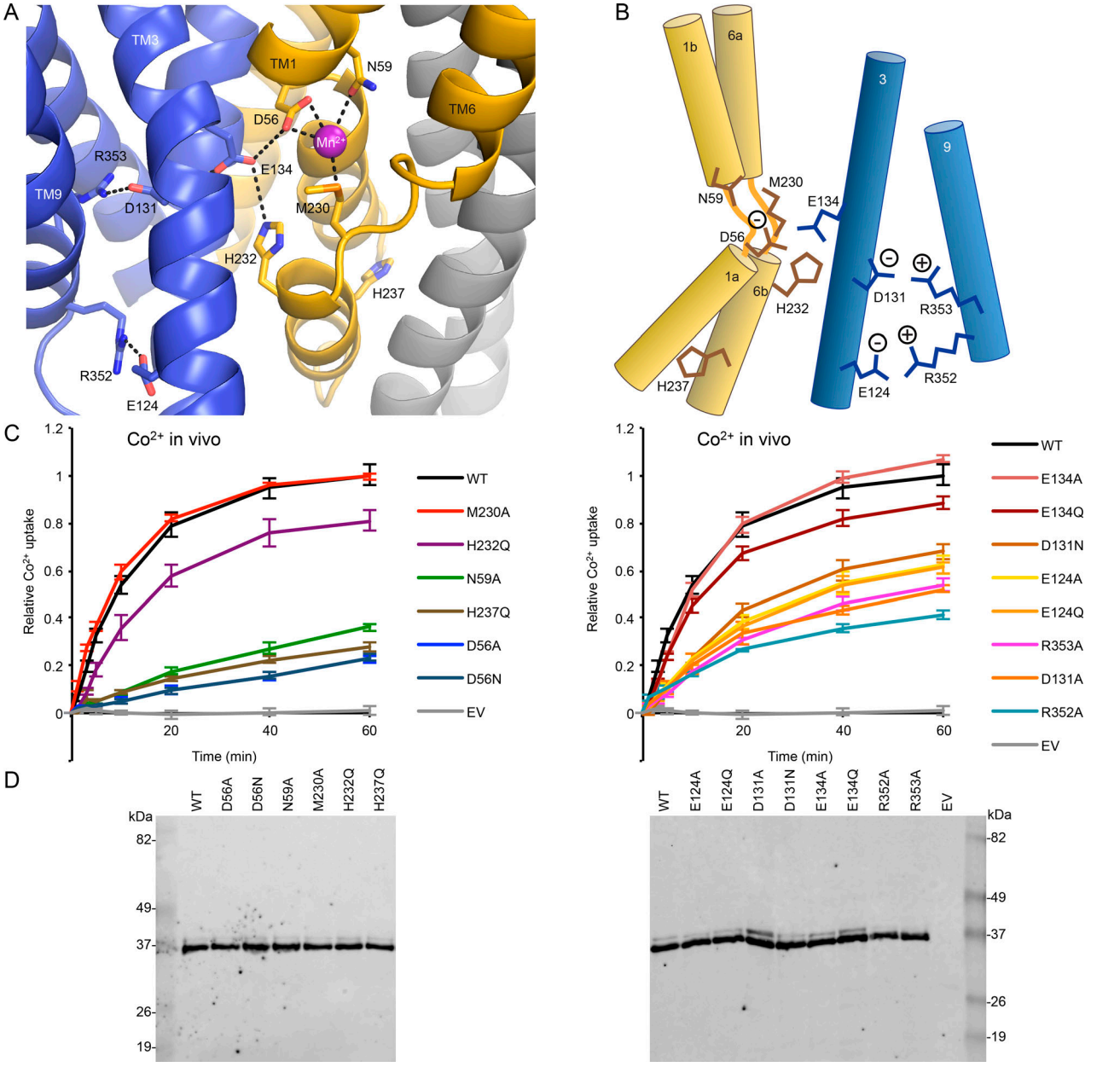

Figure S4. **Conserved charged and protonatable residues form a network leading from the metal-binding site to the cytosol. (A)** View down the metal entry pathway to the conserved network in outward-open DraNramp (PDB accession no. 6BU5). TMs 10 and 11, which abut TMs 6a and 3, have been removed for clarity. TM6b's H237 lines the metal exit pathway to the cytosol, while the rest of the network lines the proton exit route (Bozzi et al., 2019). **(B)** Schematic of the conserved residues in the salt-bridge network. **(C)** Time courses of in vivo Co^{2+} uptake at pH 7.0 and 10 mM KCl (averages ± SEM; $n = 4$). Mutants at most positions retained some Co^{2+} transport in *E. coli*, with D56, N59, and H237 mutants most impaired. **(D)** All constructs express similarly when detected via Western blot for the N-terminal His-tag.

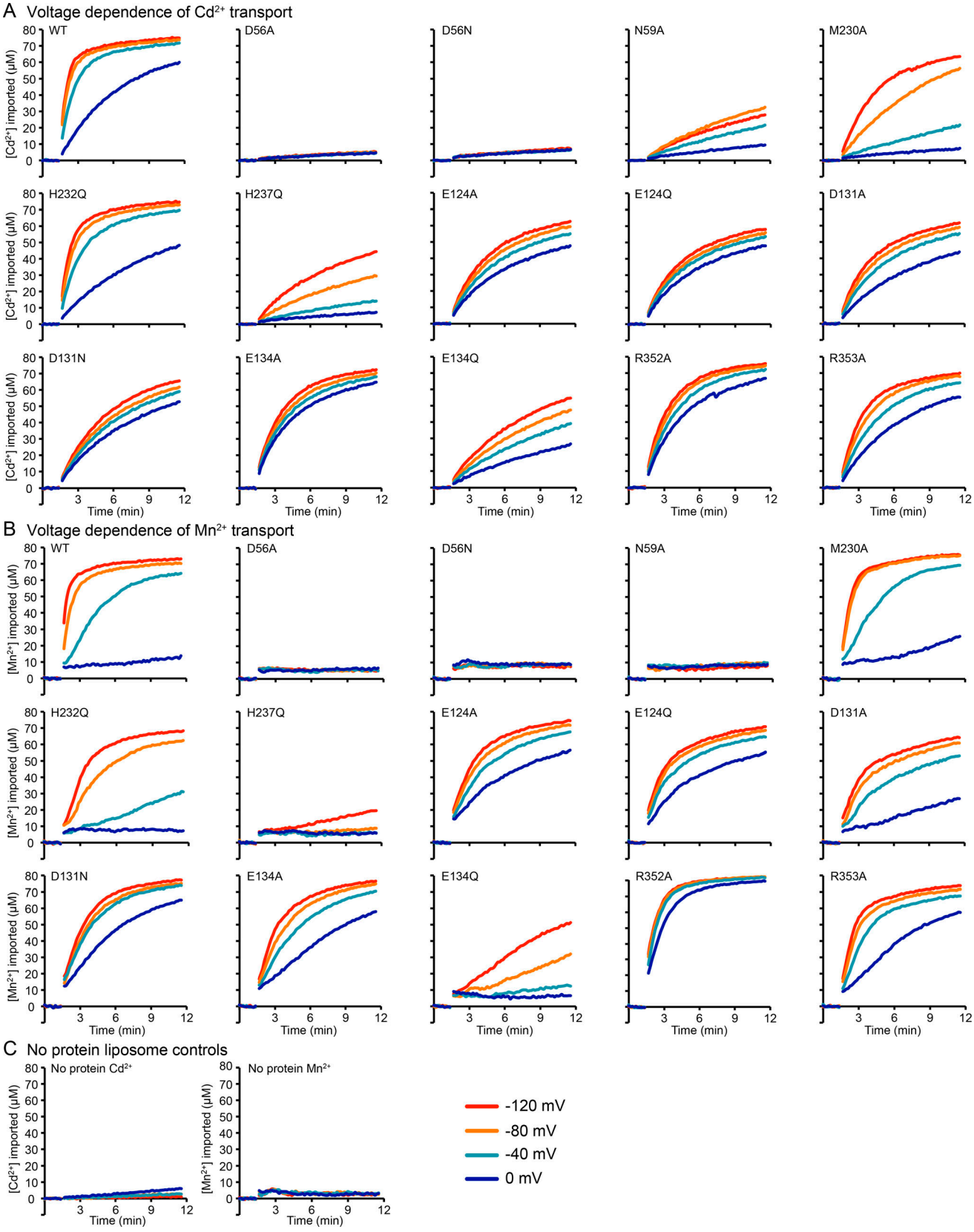

Figure S5. **Sample traces illustrate mutant perturbations to voltage dependence of metal transport rate. (A and B)** Representative time traces ($n \geq 4$) of Cd^{2+} (A) and Mn^{2+} (B) uptake into proteoliposomes measured at four ΔΨ values for each mutant. **(C)** Representative time traces ($n > 4$) of Cd^{2+} (left) and Mn^{2+} (right) uptake showed that no metal was imported into control liposomes.

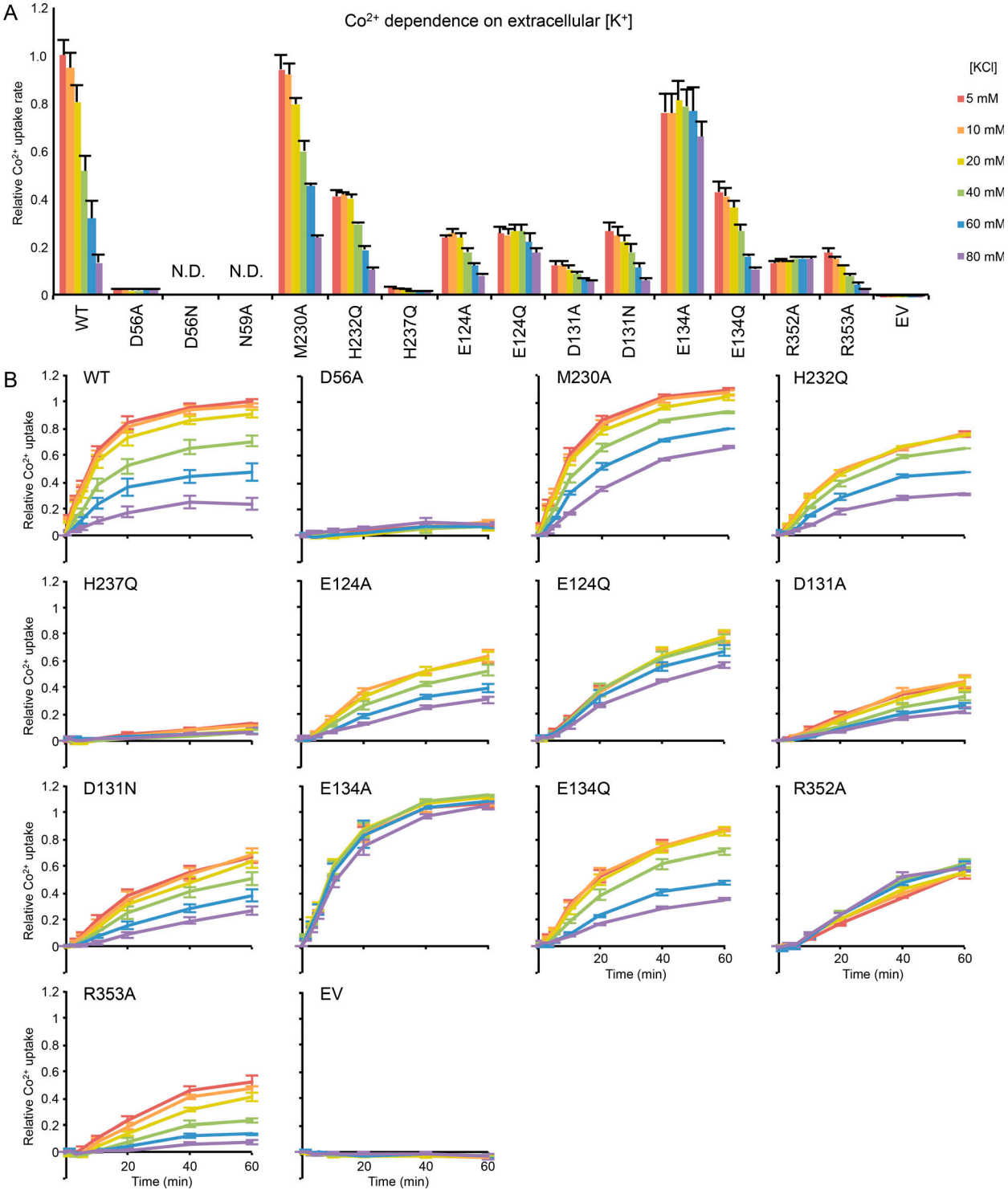

Figure S6. **Mutations to conserved residues perturb voltage dependence of in vivo Co^{2+} transport rate. (A)** Relative Co^{2+} transport rates at pH 7.0 and various extracellular [K^+] values applied to perturb the endogenous *E. coli* membrane potential; higher extracellular [K^+] presumably leads to a less negative $\Delta\Psi$. Mutations to E124, D131, E134, and R352 reduced the effect of extracellular [K^+] more than mutations to M230, H232, and R353. D56N and N59A mutants were not tested (N.D.). **(B)** Time course data used to generate the initial rates in A. All data are averages ± SEM ($n \geq 3$).

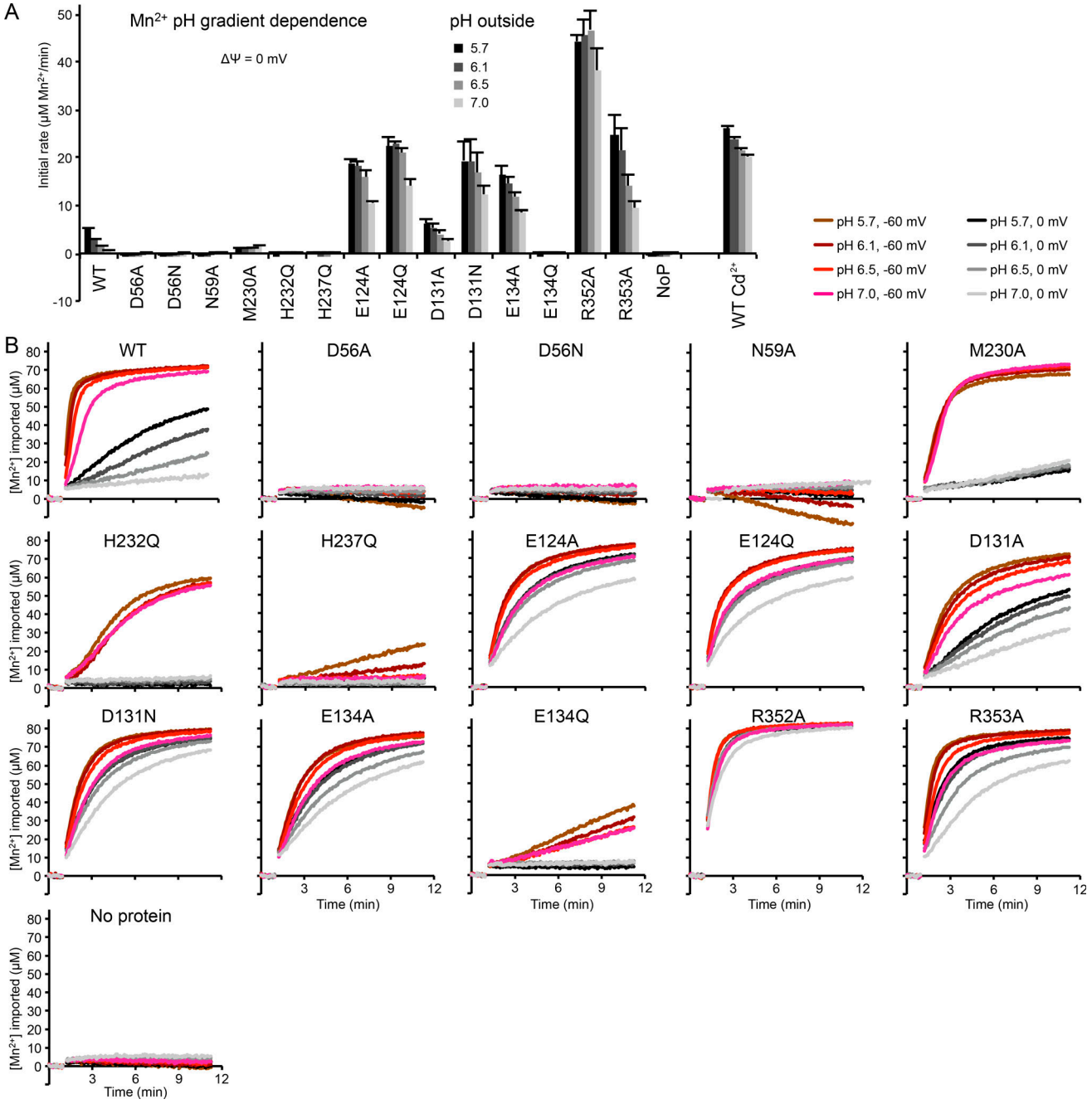

Figure S7. **Effects of mutations on ΔpH and ΔΨ stimulation of Mn^{2+} transport. (A)** Average initial Mn^{2+} transport rates ± SEM ($n \geq 4$) at various external pHs at ΔΨ = 0. E124, D131, E134, R352, and R353 mutants retained significant Mn^{2+} transport but little ΔpH dependence. Even with a ΔpH, H232Q and M230A did not transport Mn^{2+}. **(B)** Representative time traces ($n \geq 4$) of Mn^{2+} influx at four ΔpH values at ΔΨ = 0 and −60 mV for each mutant.

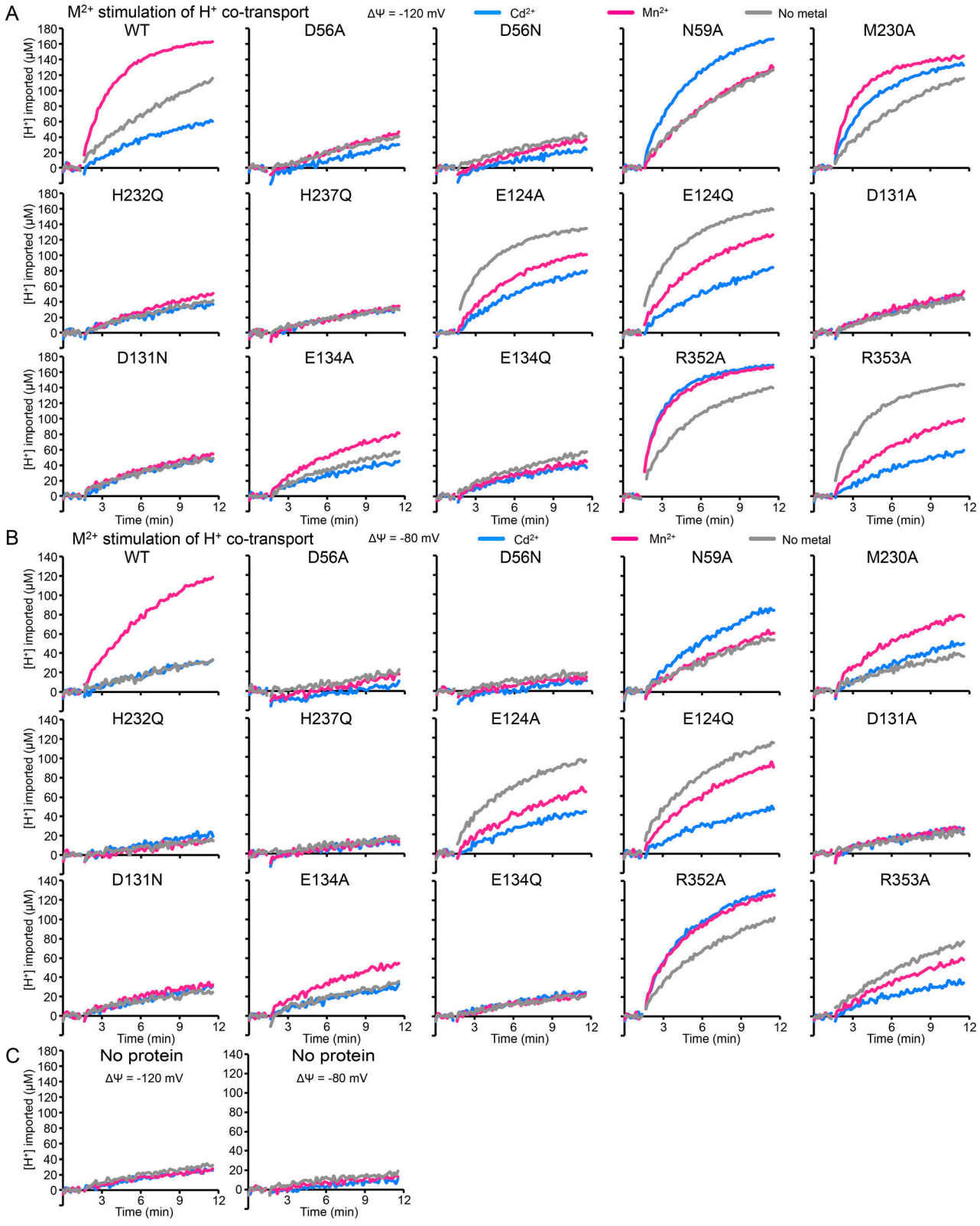

Figure S8. **Sample traces show effects of mutations on metal-stimulated H⁺ transport. (A and B)** Representative time traces ($n \geq 4$) of metal-stimulated H^+ transport in proteoliposomes at $\Delta\Psi = -120$ mV (A) or −80 mV (B). H^+ entry was measured in the absence of metal and in the presence of Mn^{2+} or Cd^{2+} for each mutant. **(C)** No significant H^+ entry was observed into control no-protein liposomes under any of the tested conditions.

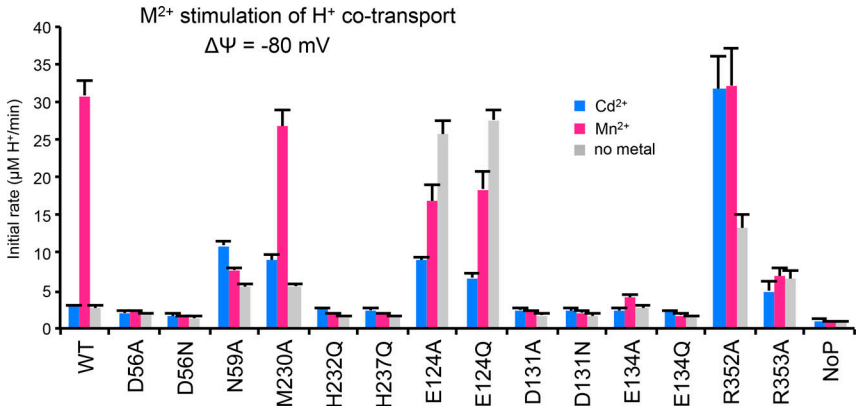

Figure S9. **Mutational effects on metal-stimulated H⁺ transport show same trend at less-negative voltage.** Average initial metal-stimulated H⁺ transport rates ± SEM ($n \geq 4$) at −80 mV with pH 7.0 on both sides of the membrane, in the absence or presence of 750 μM M^{2+}, show the same trends as at −120 mV in Fig. 8 C.

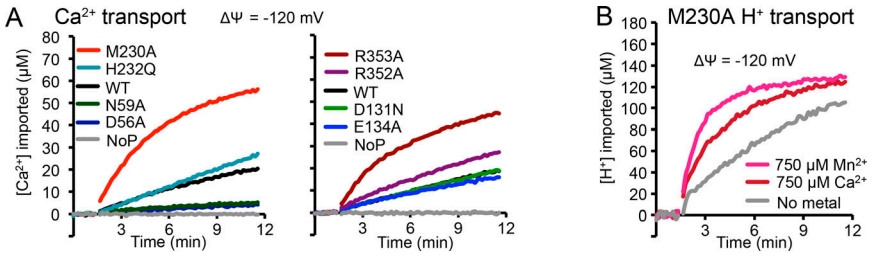

Figure S10. **Two mutations increase DraNramp Ca^{2+} transport. (A)** Representative time traces ($n \geq 4$) of Ca^{2+} uptake into proteoliposomes. M230A and R353A increased Ca^{2+} transport, D56A and N59A eliminated Ca^{2+} uptake, and other mutants behaved comparably to WT. **(B)** Representative time traces ($n = 4$) of Ca^{2+}-stimulated H⁺ uptake into proteoliposomes by M230A.

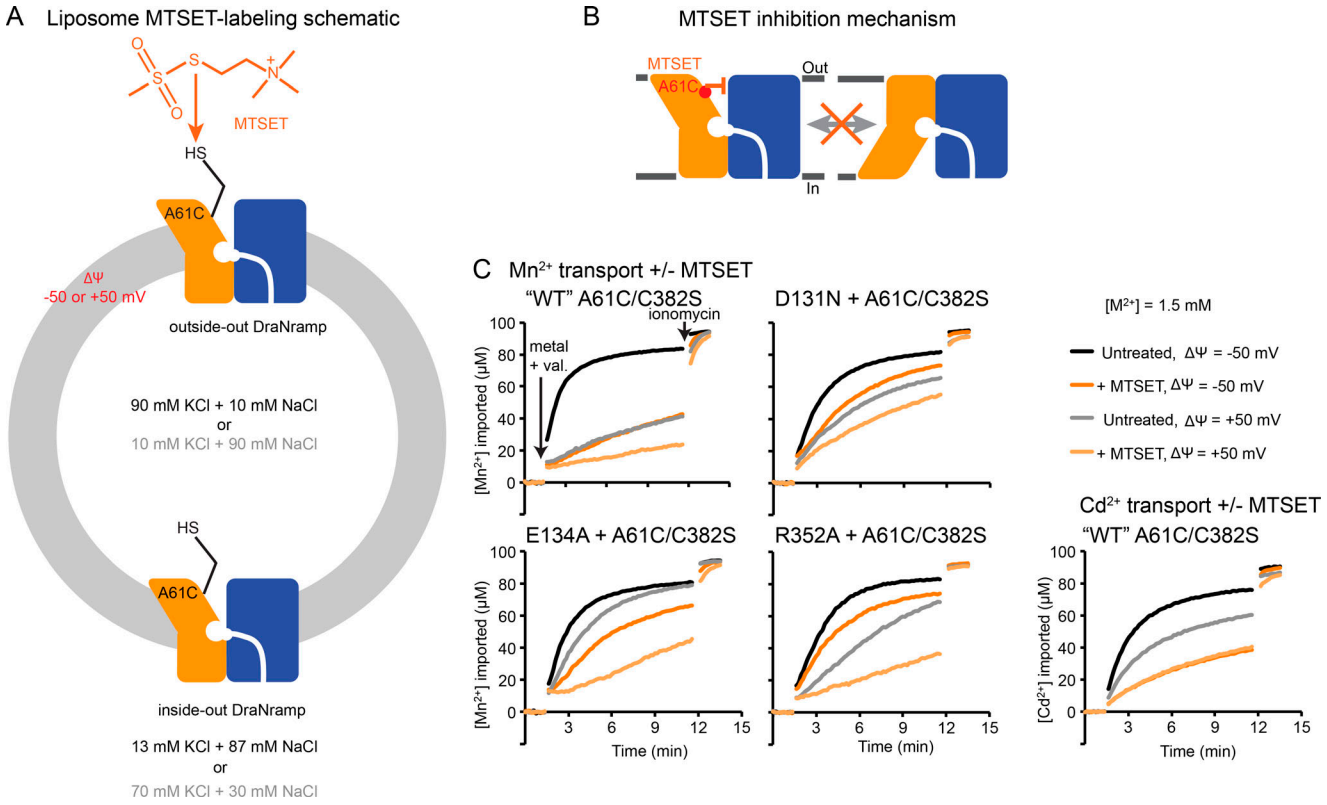

Figure S11. **Test of DraNramp back transport. (A)** Membrane-impermeable MTSET only modifies A61C of DraNramp molecules oriented outside-out after reconstitution into liposomes. Inside-out DraNramp, which accounts for ∼50% of the inserted protein (Bozzi et al., 2019), is protected from modification and thus capable of conformational cycling. **(B)** Labeling A61C with positively charged MTSET likely inhibits DraNramp metal transport by locking the protein in an outward-open conformation. **(C)** Representative metal uptake traces (n = 4) of A61C constructs at ΔΨ = −50 or +50 mV in the presence or absence of MTSET. We note that WT-like A61C/C382S does transport some Mn^{2+} at ΔΨ ≥ 0, unlike the true WT (Fig. S1 H). Mutations D131N, E134A, and R352A all had increased Mn^{2+} transport compared with WT-like at +50 mV even after MTSET labeling. In comparison to Mn^{2+}, Cd^{2+} transport by WT-like was less dependent on voltage and showed more residual transport after MTSET labeling. Addition of ionomycin shuttles divalent cations to show the maximum signal.

Table S1. **Summary of the transport kinetics results presented in Figs. 7, 8, and 9**

Mutant	Residue location	Distance to M^{2+} (Å)	Transport			ΔΨ dependent	ΔpH dependent	H^+ uniport	H^+/Mn^{2+} cotransport	Proposed role
			Cd^{2+}	Mn^{2+}	Ca^{2+}					
D56A	Metal-binding site	2.9	X	X	X	NA	NA	X	X	Metal binding, initial proton binding, ΔpH activation, voltage dependence
D56N	Metal-binding site	2.9	X	X	X	NA	NA	X	X	Metal binding, initial proton binding, ΔpH activation, voltage dependence
N59A	Metal-binding site	3.4	<<<	X	X	=	NA	=	=	Metal binding
M230A	Metal-binding site	3	<<	=	>>		X	=	=	Metal binding, substrate selectivity, ΔpH activation
H232Q	H^+-transport pathway	6.2	=	<<	=	=	X	X	X	Proton transfer, ΔpH activation, conformational change
E134A	H^+-transport pathway	5.3	<	<	=	<<	<<<	X	<<<	Proton transfer, ΔpH activation, voltage dependence
E134Q	H^+-transport pathway	5.3	<<	<<<	=	<	X	X	X	Proton transfer, ΔpH activation, voltage dependence
D131A	H^+-transport pathway	11	<	<	=	<<	<<	X	X	Secondary proton binding, voltage dependence
D131N	H^+-transport pathway	11	<	<	=	<<<	<<	X	X	Secondary proton binding, voltage dependence
R353A	H^+-transport pathway	14.7	<	<	>	<<	<<	>	Inverted	Voltage dependence, proton exit
R352A	H^+-transport pathway	17.9	<	<	=	<<<	<<<	>		Voltage dependence, proton exit
E124A	H^+-transport pathway	17.7	<	<	=	<<<	<<<	>>	Inverted	Voltage dependence, proton exit
E124Q	H^+-transport pathway	17.7	<	<	=	<<<	<<<	>>	Inverted	Voltage dependence, proton exit
H237Q	Metal-release pathway	13.4	<<<	X	X	=	=	X	X	Conformational change, metal exit

Distances to M^{2+} were determined for outward-open Mn^{2+}-bound DraNramp (PDB accession no. 6BU5). <, less than WT; =, comparable to WT; >, more than WT; NA, not applicable; X, eliminated.

References

Bozzi, A.T., C.M. Zimanyi, J.M. Nicoludis, B.K. Lee, C.H. Zhang, and R. Gaudet. 2019. Structures in multiple conformations reveal distinct transition metal and proton pathways in an Nramp transporter. *eLife.* 8:e41124. https://doi.org/10.7554/eLife.41124